

---

## Precession control of interglacial winter monsoon intensity over tropical East Asia

Huang Enqing <sup>1,\*</sup>, Wang Shihe <sup>1</sup>, Wei Sihua <sup>1</sup>, Yuan Zijie <sup>1</sup>, Tian Jun <sup>1</sup>

<sup>1</sup> State Key Laboratory of Marine Geology, Tongji University, 200092 Shanghai, China

\* Corresponding author : Enqing Huang, email address : [ehuang@tongji.edu.cn](mailto:ehuang@tongji.edu.cn)

---

### Abstract :

The history of the East Asia winter monsoon (EAWM) and its forcing mechanisms remain elusive due to conflicting reconstructions. In this study, we attempt to quantify changes in interglacial winter monsoon intensity over tropical East Asia, based on reconstructions from the southern South China Sea (SCS) and model outputs from transient simulations (TRACE-21). The new monsoon record is derived from individual-specimen  $\delta^{18}\text{O}$  of planktonic foraminifera, the variability of which is dominated by the seasonality of sea surface temperature and thus the intensity of the EAWM over the SCS. The standard deviation of individual-specimen  $\delta^{18}\text{O}$  shows a gradual decrease from 0.61 to 0.20 and from 0.49 to 0.25 across marine isotope stages (MISs) 5e and 1, respectively, indicating a decline of the EAWM intensity along with precessional changes. Reconstructions and simulations together constrain a 15% decrease of the EAWM intensity over the Holocene, and a more substantial weakening over the MIS 5e. Precessional forcing of the interglacial EAWM variations over the SCS can be mainly explained by two mechanisms. First, a persistent increasing of boreal winter insolation can reduce the temperature gradient between Asian inlands and the Pacific, weakening the entire winter wind field over East Asia. Second, precessional forcing gave rise to an increasing El Niño frequency and magnitude over the Holocene, which facilitated the establishment of an anomalous anticyclonic circulation over the tropical West Pacific and thus reduced the northerly winter winds. Contrary to traditional views, the retreat of the Northern Hemisphere ice sheets during early interglacial periods did not contribute to changes in the tropical EAWM. In addition, model outputs have also explicitly revealed that the mid-latitude and the tropical EAWM systems respond differently to a set of forcing factors, suggesting a spatial discrepancy of the EAWM evolution in the past.

### Highlights

► Reliable monsoon reconstruction based on spreading of single-specimen oxygen isotopes. ► Transient simulations give clear mechanisms for winter monsoon evolution. ► Boreal winter insolation determines wind intensity via altering temperature gradient. ► A tight correlation between tropical winter monsoon and ENSO dynamics.

---

**Keywords** : East Asia winter monsoon, Individual-specimen  $\delta^{18}\text{O}$ , El Niño, the last interglacial, Holocene

## 1. Introduction

Modern East Asia is featured with both strong summer and winter monsoons. Traditionally, orbital-scale variations of the East Asian winter monsoon (EAWM) and global ice volume are thought to be coupled since the establishment of Northern Hemisphere glaciation after ~3.3 Ma (Sun et al., 2010). The expanded Northern Hemisphere ice volume can enhance the Siberian high-pressure cell and further strengthen the northwesterly and northeasterly winter winds that sweep across eastern and southeastern Asia (Fig. 1a). Therefore, the fluctuation of ice volume and the EAWM show a strong correlation for the past 800 thousand years, both being regulated by dominant quasi-periods of 100 ka (e.g., Ding et al., 1995; Liu and Ding, 1998; Lu et al., 2003; Sun et al., 2010). Based on this rationale, the EAWM records derived from the Loess Plateau in northern China have in turn been used to reconstruct the evolution of Northern Hemisphere ice volume (Hao et al., 2012, 2015).

Owing to the large meridional coverage of the EAWM, however, mounting evidence has revealed that the EAWM variation shows a substantially spatial discrepancy. Modern observations have pointed to the need to separate the ‘northern mode’ (mid-latitude) from the ‘southern mode’ (low-latitude) of the EAWM variability on the interannual timescale, with the former showing a more sensitive response to the mid-to-high latitude atmospheric circulation system and the latter to the El Niño-Southern Oscillation (ENSO) (Chen et al., 2014; Chen et al., 2018). On the orbital timescale, a 300-ka transient simulation forced by solar insolation, greenhouse gases and ice volume also reveals a latitudinal dependence of the EAWM variability

(Xie et al., 2019). The Northern Hemisphere ice sheet plays a major role in regulating the intensity of the northern EAWM by modifying the North Pacific atmospheric circulation; while boreal winter insolation can account for the southern EAWM variations through modulating the zonal land-sea temperature gradient at low latitudes (Xie et al., 2019). Therefore, changes in the northern and the southern EAWM intensity show a dominant periodicity of 100 and 23 ka, respectively, during the late Quaternary (Xie et al., 2019).

The EAWM reconstructions derived from a variety of proxies, however, do not fully reproduce the transient simulation results as discussed above. In northern China, the EAWM records based on loess grain-size variations show a combined influence of 100, 41 and 23 ka cycles (e.g., Ding et al., 1995; Liu and Ding, 1998; Lu et al., 2003; Shi et al., 2011; Hao et al., 2012). In particular, increased obliquity (41-ka cycles) can enhance the meridional temperature gradient and further intensify the EAWM, thus leaving a strong imprint on loess records in addition to the 100-ka cycles (Shi et al., 2011). In the South China Sea (SCS), the EAWM reconstructions derived from changes in wind-driven sea surface temperature (SST) gradients suggest that the southern EAWM variability was mainly modulated by the 23-ka precession cycles (Yamamoto et al., 2013; Huang, 2015). However, they were out of phase with boreal winter insolation forcing (Yamamoto et al., 2013; Huang, 2015), which differed from the prediction of model studies (Wen et al., 2016; Xie et al., 2019).

More controversial EAWM reconstructions are from the Holocene period. Over the Loess Plateau, most grain-size records indicate a generally decreasing EAWM intensity from the early to the late Holocene (e.g., Sun et al., 2006; Stevens et al., 2007; Yang and Ding 2014; Li et al., 2021). In contrast, a recent grain-size stack suggests that the northern EAWM variations could be divided into two stages centered around 6.5 ka BP, with a weakening trend in the early-to-mid Holocene and a strengthening trend in the mid-to-late Holocene (Kang et al., 2020). Furthermore, the late Holocene EAWM intensity (2-0 ka BP) was inferred to be even stronger than the

early Holocene (12-10 ka BP, Kang et al., 2020). In southern China and the SCS, the majority of reconstructions reveal a persistent decrease in the EAWM intensity over the Holocene, along with an increasing boreal winter insolation (Huang et al., 2011; Steinke et al., 2011; Wang et al., 2012; Jia et al., 2015). However, exceptional records also exist. A high-resolution SST record from the northern SCS suggests an increasing influence of coastal cold-water masses and a strengthening of the EAWM since 7.0 ka BP (Zhang et al., 2019).

To summarize, although there is a growing consensus that the EAWM variation shows spatial heterogeneity, conflicting reconstructions hinder attempts to discern this spatial pattern and the underlying mechanisms. The presence of these controversial EAWM records is partly due to the fact that some proxies are substantially influenced by other climatic and geological processes rather than by monsoon changes. In this study, we provide a new winter monsoon record for the Marine Isotope Stages (MISs) 5e and 1, based on changes in individual-specimen foraminiferal  $\delta^{18}\text{O}$  from the southern SCS (Fig. 1). We further use transient climate simulation results from the Community Climate System Model 3 (CCSM3 Liu et al., 2009; Wen et al., 2016) to analyze major causes for interglacial EAWM variations.

## **2. Regional setting**

### **2.1 Seasonal climate change of the SCS**

Changes in the SCS surface conditions are highly sensitive to the seasonal reversal of monsoon wind field. From May to August, the southwesterly summer monsoon winds can drive a basin-scale anticyclonic circulation, which generates a nearly homogenous sea surface temperature (SST) distribution with a mean value of  $\sim 28.5^\circ\text{C}$  over the entire SCS (e.g., Shaw and Chao, 1994; Chu and Wang, 2003; Fig. 1b). From November to February, the intense winter monsoon winds deliver cold surface waters from the northern SCS to the south, giving rise to a strong western boundary current along the Vietnamese coast and a distinct cold surface area (referred to as the ‘cold tongue’) in the southwestern SCS (Chu et al., 1999; Liu et al., 2004; Fig. 1a and 1c).

Moreover, the northeasterly winter wind can generate a prominent winter SST gradient between the northern and southern SCS as well as between the southwestern and southeastern SCS (Liu et al., 2004; Huang et al., 2011; Fig. 1a and 1c). These SST gradients have fluctuated between 2.4-4.1°C and 0.9-1.8°C, respectively, in the past several decades (Huang et al., 2011; Huang, 2015).

Owing to the southward advection of cold waters and the presence of ‘cold tongue’ during winter time, seasonal SST changes in the southwestern SCS are largely determined by the winter monsoon intensity. As illustrated in Fig. 2a, the SST difference between summer (June-July-August, JJA) and winter (December-January-February, DJF) seasons at our study site (MD05-2896/97, Fig. 1b) shows an evident correlation with the DJF meridional wind speed between 1949 and 2022 ( $R=-0.69$ ,  $n=74$ ,  $p<0.00001$ ). The strengthened winter monsoon winds can intensify and expand the ‘cold tongue’ area, thereby lowering winter SSTs and increasing the seasonal SST difference (Liu et al., 2004; Huang et al., 2011).

Previous studies have also noticed a correlation between the SCS winter wind intensity and the ENSO on an interannual timescale (Liu et al., 2004; Huang et al., 2011; Zhao et al., 2019). Indeed, recent observations have confirmed this link. Between 1949 and 2022 the DJF wind speed variability over the SCS is strongly correlated with the SST fluctuation in the Niño 3.4 region ( $R=0.61$ ,  $n=74$ ,  $p<0.00001$ , Fig. 2b). Particularly, strong El Niño years of 1972/1973, 1997/1998 and 2009/2010 were associated with an unusually weak winter monsoon over the SCS (Fig. 2b). This is because the El Niño phase can drive an anomalous anticyclonic circulation over the Indo-Western Pacific (Liu et al., 2004; Huang et al., 2011; Zhao et al., 2019), thus weakening the northeasterly winter winds to the SCS and further reducing the spread of the ‘cold tongue’ as well as the seasonal SST contrast at our core location (Fig. 2).

## 2.2 Climate significance of seasonal changes in planktonic foraminiferal $\delta^{18}\text{O}$

Plankton-tow investigations have demonstrated that *Globigerinoides ruber* is a mixed

layer-dwelling species in the SCS (e.g., Lin et al., 2011; Luo et al., 2015). Sediment-trap records from the central and the southern SCS have further shown that the flux of *G. ruber* is considerably increased during both the summer and winter monsoon seasons, corresponding to relatively high sea-surface chlorophyll concentrations, but decreased during the inter-monsoon seasons (Fig. 3a; Chen et al., 2007; Wan et al., 2010). This bimodal pattern found in the species-specific flux suggests that the flourishing and the deposition of *G. ruber* in the tropical SCS does not have a single-season preference. Moreover, sediment-trap records reveal that seasonal *G. ruber*  $\delta^{18}\text{O}$  variations closely follow SST changes in our study area (Fig. 3b and 3c, Wan et al., 2010). The mean seasonal SST change of 2.98°C corresponds to that of the *G. ruber*  $\delta^{18}\text{O}$  variation of 0.52‰ (Fig. 3b and 3c). Therefore, SST changes can fully account for shifts in  $\delta^{18}\text{O}$ , given the conversion of  $\sim 0.23\text{‰}$  per degree between *G. ruber*  $\delta^{18}\text{O}$  and temperature (Muller et al., 2003).

Because a single specimen of *G. ruber* can only live for a couple of weeks, the  $\delta^{18}\text{O}$  variance of individual specimens from a sediment sample can therefore record changes in ocean surface conditions on seasonal to interannual time scales (e.g., Sadekov et al., 2013; Groenewald et al., 2019). According to modern observations in the southern SCS (Figs. 2 and 3), we believe that the  $\delta^{18}\text{O}$  variance of individual specimens can faithfully reflect seasonal SST changes, and it can further indicate changes in winter wind speeds over the SCS.

### 3. Material and Methods

#### 3.1 Core MD05-2896 and 2897

Sediment cores MD05-2896 (08°49.05'N, 111°26.47'E; water depth, 1657m; core length, 11.03 m) and MD05-2897 (08°49.53'N, 111°26.51'E; water depth, 1658 m; core length, 30.98 m) were retrieved from the southern SCS during the MD147-Marco-Polo Cruise (Fig. 1, Laj et al., 2005). The core material consists of clay or silty clay with abundant calcareous fossils. The uppermost part of core MD05-2897 was lost during coring process. This missing section covers a

sedimentary history from the Last Glacial Maximum to the Holocene, which is supplemented by material from the adjacent core MD05-2896 in this study (Fig. 4).

### 3.2 Stable oxygen and carbon isotope of foraminifera

Sample preparation and analyses were performed at the State Key Laboratory of Marine Geology, Tongji University. Planktonic foraminifera *G. ruber* (sensu stricto, white, size fraction 300-360  $\mu\text{m}$ , measured along the longest shell axis) and benthic foraminifera *Cibicidoides wuellerstorfi* (size fraction  $>400 \mu\text{m}$ ) were picked for carbonate  $\delta^{18}\text{O}$  and  $\delta^{13}\text{C}$  measurements. For the individual-specimen analysis, foraminiferal shells were ultrasonically cleaned in ethanol. For the pooled-specimen analysis, foraminiferal shells were crushed into large fragments and homogenized before being ultrasonically cleaned in ethanol. All samples were analyzed using a Finnigan MAT 253plus mass spectrometer coupled to an automatic Kiel-IV carbonate preparation device. Measurement results were converted to the international Pee Dee Belemnite (PDB) scale. Long-term replicate measurements of an international carbonate standard show a standard deviation of  $\pm 0.04\text{‰}$  and  $\pm 0.08\text{‰}$  for  $\delta^{18}\text{O}$  and  $\delta^{13}\text{C}$  analysis, respectively. Approximately 36-50 specimens from each sample and a total of 23 samples were used for individual-specimen  $\delta^{18}\text{O}/\delta^{13}\text{C}$  analyses, and 889  $\delta^{18}\text{O}$  data points were obtained (Table 1, supplementary data file). For pooled-specimen  $\delta^{18}\text{O}/\delta^{13}\text{C}$  analyses, *G. ruber* and *C. wuellerstorfi* samples were measured every 2 and 4-8 cm, respectively, equivalent to an average time resolution of 210 and 750 years (supplementary data file).

### 3.3 Statistical Methods

In each array of the individual-specimen  $\delta^{18}\text{O}$  dataset, outliers were recognized using the  $1.5\times$ interquartile range criterion. This resulted in the removal of 20 data points ( $\sim 2.2\%$  of all data) from the final results. We further test the individual-specimen  $\delta^{18}\text{O}$  distribution for normality using the Lilliefors Test. For 3 out of 23 samples, the null hypothesis that the measurements are normally distributed is rejected ( $P < 0.05$ , Table 1). Accordingly, the majority of samples fit a normal distribution, and the standard



deviation can be used to characterize the spread of the individual-specimen  $\delta^{18}\text{O}$  data.

### 3.4 The TRACE-21 simulation

The TRACE21 is a transient simulation of global climate change for the past 21,000 years, performed using a coupled atmosphere-ocean-land surface-sea ice model with a dynamic vegetation module (CCSM3). A series of experiments have been conducted that are forced by a single factor, including atmospheric greenhouse gas concentrations, orbital parameters, continental ice volume and meltwater fluxes (single-forcing experiments), and also forced by an integration of these factors (integrated experiment) (e.g., Liu et al., 2009, 2014). In this way, the main drivers for a specific climate change process are expected to be identified. Published model outputs are broadly consistent with proxy reconstructions and have successfully reproduced many important features of climate change from regional to global scales (e.g., Liu et al., 2014; Wen et al., 2016). Model results are accessible to the scientific community on the website of the National Center for Atmospheric Research (<https://www.earthsystemgrid.org/project/trace.html>). In this study, simulated changes in the EAWM and their forcing mechanisms are analyzed and compared with our proxy records.

## 4. Results

### 4.1 Age model

In previous studies, a total of 13 accelerator mass spectrometry (AMS)  $^{14}\text{C}$  dating were used to establish the chronostratigraphy of the upper 3 meters of core MD05-2896 (Fig. 4a; Tian et al., 2010; Wan and Jian, 2014). For the upper part of core MD05-2897, 4 AMS  $^{14}\text{C}$  dating and the radiometric dating results of the “Youngest Toba Tuff” were used to constrain the age model (Huang and Tian, 2012). In this study, the age model for the depth interval between 424-1165 cm of core MD05-2897 was further constructed by linking the benthic foraminiferal  $\delta^{18}\text{O}$  record to the global benthic  $\delta^{18}\text{O}$  stack (LR04, Lisiecki and Raymo, 2005) through visual correlation (Fig. S1). The *C. wuellerstorfi*  $\delta^{18}\text{O}$  of core MD05-2896/97 oscillates

between 2.2‰ and 4.2‰ over the past 160 ka and shows a clear division of marine isotope stages/substages (Figs. 4a and S1). All age control points of the two cores are listed in Table S1. MISs 1 and 5e are constrained in depth intervals of 0-87 and 919-982 cm in cores MD05-2896 and 2897, respectively (Fig. 4a), with mean sedimentation rates of 7.6 and 6.9 cm/ka.

#### 4.2 Standard deviation of individual-specimen $\delta^{18}\text{O}$

As illustrated in Fig.4, the means of the individual-specimen  $\delta^{18}\text{O}$  measurements are generally in agreement with the pooled-specimen  $\delta^{18}\text{O}$  results, except for two samples between 12 and 11 ka BP. Individual-specimen  $\delta^{18}\text{O}$  data range from -4.80‰ to -1.61‰ and from -4.40‰ to -1.22‰, respectively, during the MISs 5e and 1. We fit a third-degree polynomial curve to the standard deviation of individual-specimen  $\delta^{18}\text{O}$  measurements, in order to better constrain the trend and the magnitude of changes (Figs. 4c and 4e). The standard deviation shows a decreasing trend from 0.61 to 0.20 and from 0.49 to 0.25 across the MISs 5e and 1, respectively, consistent with contemporary changes in precession (Laskar et al., 2011). We also note that the magnitude of the change in standard deviation is 30% greater during the MIS 5e compared to the MIS1, corresponding to a 1.3-fold greater change in precession.

### 5. Discussion

#### 5.1 The southern EAWM during MISs 5e and 1

Based on modern observations, the extent of the individual-specimen  $\delta^{18}\text{O}$  spread is mainly determined by the seasonal SST contrast and thus the winter wind speed in the southern SCS (Figs. 2 and 3). Therefore, changes in the standard deviation of individual-specimen  $\delta^{18}\text{O}$  measurements can in turn be used to indicate the southern EAWM variations. This new winter monsoon record is consistent with previous reconstructions based on the west-east SST gradient in the southern SCS (Fig. 5b; Huang et al., 2011) and the upper ocean thermal gradient in the northern SCS (Steinke et al., 2011). All three of these proxy records are relevant to large-scale wind field changes over the broad open SCS, and are thus robust documents for the history of the

southern EAWM. Together they reveal a gradual decrease in monsoon intensity over the Holocene period. Furthermore, new data from the MIS 5e suggest that this decreasing trend is temporally recurrent across interglacial peaks, and the MIS 5e experienced a more pronounced change in winter wind speeds compared to the Holocene.

In contrast, other winter monsoon reconstructions from the SCS and the Sulu Sea imply a different story. The EAWM reconstructions based on changes in planktonic foraminiferal faunal assemblages or sea-surface productivity suggest a strong control of ice volume on the long-term evolution of the winter monsoon intensity (Chen and Huang, 1998; de Garidel-Thoron et al., 2001). For the Holocene period, they suggest a strengthening or unchanged trend (Chen and Huang, 1998; de Garidel-Thoron et al., 2001). However, changes in foraminiferal faunal assemblages are substantially influenced by regional SST fluctuations. In addition, the SCS is surrounded by vast continental shelves. Sea-level fluctuations can induce dramatic advance and retreat of coastlines, which further affect terrigenous nutrient inputs to marine core locations and the reconstructed sea-surface productivity. As a result, these two sets of records are considerably influenced by non-monsoon processes, which are not “pure” proxies for the winter wind speed.

Another record, based on changes in coastal SST in the northern SCS, is also thought to indicate a strengthening of the EAWM since the mid-Holocene (Zhang et al., 2019). However, compared to monsoon reconstructions from the open ocean, coastal records are suspected to be influenced by changes in local hydrological processes along with the sea-level rising and the drowning of the continental shelf. Shifts in the direction and the extension of coastal currents can bias the interpretation of coastal SST records in terms of monsoon wind changes. To summarize, despite the existence of conflicting reconstructions from the SCS, winter monsoon records based on the seasonal SST contrast (this study) and the thermal gradient in the SCS (Huang et al., 2011; Steinke et al., 2011) seem the most reliable based on the strong support of modern

observations.

## 5.2 Precession control of southern EAWM changes over interglacial periods

We use model outputs from the TRACE-21 experiments to identify the forcing mechanisms for changes in the southern EAWM. As shown in Fig. 6a, simulated changes in the winter meridional wind speed over the SCS, derived from the integrated experiment, show an increasing trend from 6.7 m/s to 7.2 m/s (absolute values) between 14.0-8.6 ka BP and a decreasing trend from 7.2 m/s to 6.3 m/s between 8.6-0.7 ka BP. This is broadly consistent with our proxy reconstructions. Previously, it has been reported that simulated winter wind speeds also match with another proxy record based on the west-east SST gradient in the southern SCS (Fig. 5b; Huang et al., 2011; Wen et al., 2016). Therefore, model simulations and data reconstructions collaborate to confirm a weakening history of the southern EAWM history over the Holocene. Moreover, the model outputs provide a constraint on the magnitude of monsoon decline, which is around 15% across the Holocene.

Compared with model outputs from single-forcing experiments, it is clear that orbital forcing is mainly responsible for the Holocene changes in the southern EAWM (Fig. 6b). With respect to the late Holocene, a closer northern hemisphere winter to aphelion and reduced boreal winter insolation (Fig. 5e; Laskar et al., 2011) resulted in a cooling of the Asian winter inlands during the early Holocene. This further strengthened the Siberian high-pressure system and increased the meridional and zonal temperature gradients between East Asia and the Pacific, which ultimately caused stronger northerly winds flowing across East Asia and the associated marginal seas (Fig. 7, Tian and Jiang, 2008; Wen et al., 2016; Li et al., 2021). This explanation can be extended to the MIS 5e, since the MISs 5e and 1 have similar climate background conditions in terms of changes in orbital configurations, greenhouse-gas concentrations and global ice volume (e.g., Petit et al., 1999; Waelbroeck et al., 2002; Laskar et al., 2011). Stronger precession and winter insolation forcing over the MIS 5e had caused a more substantial change in the intensity of the southern EAWM (Fig.

4e). Indeed, long-term transient simulations have also verified this inference that precession is accounted for changes in winter wind speeds over subtropical East Asia during several recent interglacial peaks (Xie et al., 2019).

### 5.3 ENSO and the southern EAWM

As aforementioned, ENSO dynamics are closely linked to the SCS winter wind speeds on interannual time scales (e.g., Liu et al., 2004; Huang et al., 2011; Zhao et al., 2019). Here we attempt to test whether this link also functions on orbital time scales. Reconstructions of the Holocene ENSO activity remain controversial (Lu et al., 2018). One set of records suggests that both the amplitude and frequency of El Niño events have gradually increased since the early Holocene (Fig. 5f, e.g., Moy et al., 2002; Conroy et al., 2008; Barr et al., 2019); while the other set of reconstructions implies that El Niño activity was attenuated during the mid-Holocene, but strong during both the early and late Holocene (e.g., Koutavas and Joanides, 2012; Cobb et al., 2013; Zhang et al., 2014). Nevertheless, it is generally accepted that El Niño activity was less variable during the early Holocene relative to the late Holocene (Zhang et al., 2014).

ENSO activity in the integrated experiment of the TRACE-21 is consistent with the first set of data reconstructions, showing a continuous increase in both frequency and magnitude over the Holocene (Fig. 5g, Liu et al., 2014). This was achieved by enhanced positive ocean-atmosphere feedbacks that occurred in the tropical Pacific in response to precessional forcing (Liu et al., 2014). In the model outputs, the reduced and muted El Niño activity during the early Holocene triggered an anomalous cyclonic circulation over the tropical western Pacific, which augments the northerly winter winds in the SCS (Fig. 7b). Therefore, ENSO dynamics seems to impact the southern EAWM intensity through similar mechanisms both on interannual and orbital time scales. A previous study argued that strong El Niño activity can induce an anomalous anticyclonic and cyclonic circulation over the SCS and the East China Sea-Okinawa Trough, respectively, leading to contrasting Holocene EAWM changes

in these two regions (Zhao et al, 2019). However, the TRACE-21 simulation does not fully support this inference, as no anomalous circulation was observed for the East China Sea-Okinawa Trough region (Fig. 7b).

At present, reliable reconstructions of ENSO activity with monthly to interannual resolution are still scarce for the MIS 5e. Therefore, the ENSO activity for this period remains poorly understood, but changes in the mean climate state over the equatorial Pacific are relatively better known. A convergence of evidence suggests that long-term fluctuations of El Niño/La Niña-like climate conditions were controlled by equatorial fall insolation during the late Quaternary (e.g., Clement et al., 1999; Dang et al., 2014; Carolin et al., 2016). Absolutely-dated stalagmite  $\delta^{18}\text{O}$  records from Borneo, controlled by the ENSO-induced atmospheric convection and precipitation over the tropical West Pacific, reveal a moderate shift to more La Niña-like climate conditions between 127 and 117 ka (Carolin et al., 2016). This corresponds to a weakening of the southern EAWM inferred from the individual-specimen  $\delta^{18}\text{O}$  record (Fig. 4e), which thus does not follow the pattern observed for the Holocene. Here we argue that probably El Niño/La Niña activity, in terms of fluctuations in frequency and magnitude, rather than shifts in the mean climate state, is likely to contribute to changes in the southern EAWM changes. Therefore, testing for the link between ENSO dynamics and the southern EAWM over the MIS 5e requires the ENSO reconstructions on the interannual time scales. Taken together, it appears that the precession control of the southern EAWM changes during interglacial periods was achieved via two mechanisms, altering the land-sea temperature contrast and modulating ENSO activity.

#### **5.4 Limited influence of ice-volume forcing for the southern EAWM evolution**

Global sea-level rose by ~60 meters between 12.0-0.0 ka BP, mainly due to the melting of the North American and Eurasian ice sheets (e.g., Lambeck et al., 2014). This sea-level rise accounted for half of the total glacial-interglacial change. Previously, the presence of residual ice sheets during the early Holocene was

considered as an important reason for the intensification of the EAWM (e.g., Huang et al., 2011; Steinke et al., 2011; Kang et al., 2020; Li et al., 2021), because it could enhance the Siberian high-pressure system and further intensify northerly winds (Wen et al., 2016; Xie et al., 2019). However, the ice-volume-only forced experiment reveals that the deglacial retreat of the Northern Hemisphere ice sheets corresponds to a continuous increase in the southern EAWM between 14.0 and 10.0 ka BP (Fig. 6b), contrary to previous thought.

Long-term EAWM reconstructions and the transient simulations further show a limited influence of ice-volume dynamics on the southern EAWM throughout the last glacial-interglacial cycle (Huang et al., 2011; Wen et al., 2016; Xie et al., 2019). The southern EAWM intensity during the Last Glacial Maximum was comparable to that during the late Holocene (Huang et al., 2011), despite the fact that most of the Northern Hemisphere ice sheets have since melted. We infer that the influence of ice volume on the East Asian subtropical winter wind field was likely masked by changes in the low-latitude atmospheric circulation, driven by ENSO dynamics as discussed above.

In addition, the role of the other two forcing factors has been assessed in the model simulation. Like ice-volume forcing, greenhouse-gas forcing has played a limited role in modulating the southern EAWM since the LGM (Wen et al., 2016). Changes in meltwater fluxes affect the southern EAWM intensity on millennial timescales rather than on orbital timescales (Wen et al., 2016). Therefore, orbital-scale variations of the southern EAWM since the last glacial can be largely ascribed to precession forcing.

### **5.5 Spatial discrepancy of the Holocene EAWM evolution**

Inconsistent loess grain-size records prevent a comparison between the history of the northern and southern EAWM. The majority of reconstructions suggest a gradual weakening of the northern EAWM over the Holocene (e.g., Sun et al., 2006; Stevens et al., 2007; Yang and Ding 2014; Li et al., 2021). If this were correct, there would

appear to be no spatial discrepancy for the Holocene. However, based on the TRACE-21 simulations, the mechanisms for winter monsoon changes in these two regions are different. In addition to the precessional forcing, the retreat of the Northern Hemisphere ice sheets as well as the greenhouse-gas forcing also contribute to the Holocene weakening of the northern EAWM (Wen et al., 2006; Li et al., 2021). Particularly, these two forcing factors become dominant during the early Holocene period (Li et al., 2021).

In contrast, if we adopt the recent loess grain-size stack published by Kang et al. (2020), then the northern and the southern EAWM show an explicitly different history over the Holocene. The two-stage evolution of the northern EAWM, first decreasing during the early-to-mid Holocene and later increasing during the mid-to-late Holocene (Fig. 5d), is ascribed to the influence of ice volume and the meridional temperature gradient, respectively (Kang et al., 2020). However, a peak in winter monsoon intensity during the latest part of the Holocene (Fig. 5d) has not been reproduced in any transient or equilibrium model simulations (Wen et al., 2016; Tian and Jiang, 2018). We note that some authors have questioned the influence of human activities on the coarsening of loess grain size in the mid-to-late Holocene (Li et al., 2021). Therefore, long-term and reliable EAWM reconstructions from widely-distributed sites are still needed to recognize the spatial pattern of winter monsoon evolution.

## 6. Conclusions

We generate a new EAWM record based on individual-specimen  $\delta^{18}\text{O}$  of planktonic foraminifera from the southern SCS, which reveals a gradual weakening of monsoon wind speeds over both the MISs 5e and 1. The interpretation of this new record is strongly supported by modern observations and model simulations, and it is consistent with most of other Holocene monsoon reconstructions from South China and the SCS. Therefore, our new data provide a robust document of interglacial changes in the EAWM. Combined with transient simulation results from the TRACE-21 experiments, the EAWM intensity over the SCS is estimated to have decreased by 15% over the



Holocene, and it experienced a more substantial reduction over the MIS 5e.

The model outputs also give the reasons for the southern EAWM variation during the two interglacial periods. A continuous increase in boreal winter insolation can reduce the temperature difference between the Asian interior and the Pacific, which combined with an increasing El Niño activity in terms of frequency and magnitude, contributes to a decreasing EAWM intensity over the SCS. In addition, model studies have explicitly revealed that the northern and the southern EAWM respond differently to external and internal forcing, resulting in the spatial discrepancy in the EAWM evolution. To decipher this spatial discrepancy, long-term and reliable EAWM reconstructions from different regions are still needed.

### **Acknowledgements**

We thank the IPEV group and the scientific party of the IMAGES cruises MD147 Leg 1-MARCO POLO. We also thank Xiaoying Jiang for laboratory assistance and two referees for constructive comments. This research is funded by the NSFC (Nos. 42122042, 42076061, 42188102, 42030403) and the Fundamental Research Funds for the Central Universities (No. 22120220531).

### **References**

- Barr, C., Tibby, J., Leng, M.J., Tyler, J.J., Henderson, A.C.G., Overpeck, J.T., Simpson, G.L., Cole, J. E., Phipps, S. J., Marshall, J. C., McGregor, G. B., Hua, Q., McRobie, F. H., 2019. Holocene El Niño-southern Oscillation variability reflected in subtropical Australian precipitation. *Sci. Rep.* 9, 1–9. <https://doi.org/10.1038/s41598-019-38626-3>.
- Carolin, S.A., Cobb, K.M., Lynch-Stieglitz, J., Moerman, J.W., Partin, J.W., Lejau, S., Malang, J., Clark, B., Tuen, A.A., Adkins, J.F., 2016. Northern Borneo stalagmite records reveal West Pacific hydroclimate across MIS 5 and 6. *Earth Planet. Sci. Lett.* 439, 182–193. <https://doi.org/10.1016/j.epsl.2016.01.028>.
- Chen, M. T., Huang, C.Y., 1998. Ice-volume forcing of winter monsoon climate in the

- South China Sea. *Paleoceanography* 13, 622–633.  
<https://doi.org/10.1029/98PA02356>.
- Chen, R., Wiesner, W.M., Zheng, Y, Cheng, X., Jin, H., Zhao, Q., Zheng, L., 2007. Seasonal and annual variations of marine sinking particulate flux during 1993~1996 in the central South China Sea. *Acta Oceanol. Sin.* 26, 33–43.
- Chen, X., Li, C., Li, X., Liu, M., 2018. The northern and southern modes of East Asian winter monsoon and their relationships with El Niño-Southern Oscillation. *Int. J. Climatol.* 38, 4509–4517. <https://doi.org/10.1002/joc.5683>.
- Chen, Z., Wu, R., Chen, W., 2014. Distinguishing interannual variations of the northern and southern modes of the east Asian winter monsoon. *J. Climate* 27, 835–851. <https://doi.org/10.1175/JCLI-D-13-00314.1>.
- Chu, P.C., Edmons, N.L., Fan, C., 1999. Dynamical mechanisms for the South China Sea seasonal circulation and thermohaline variabilities. *J. Phys. Oceanogr.* 29, 2971–2989.  
[https://doi.org/10.1175/1520-0485\(1999\)029<2971:DMFTSC>2.0.CO;2](https://doi.org/10.1175/1520-0485(1999)029<2971:DMFTSC>2.0.CO;2).
- Chu, P.C., Guihua, W., 2003. Seasonal variability of thermohaline front in the central South China Sea. *J. Oceanogr.* 59, 65–78.  
<https://doi.org/10.1023/A:1022868407012>.
- Clement, A.C., Seager, R., Cane, M.A., 1999. Orbital controls on the El Niño/Southern Oscillation and the tropical climate. *Paleoceanography* 14, 441–456. <https://doi.org/10.1029/1999PA900013>.
- Cobb, K.M., Westphal, N., Sayani, H.R., Watson, J.T., Di Lorenzo, E., Cheng, H., Edwards, R.L., Charles, C. D., 2013. Highly variable El Niño-Southern Oscillation throughout the Holocene. *Science* 339, 67–70. <https://doi.org/10.1126/science.122824>.
- Conroy, J.L., Overpeck, J.T., Cole, J.E., Shanahan, T.M., Steinitz-Kannan, M., 2008. Holocene changes in eastern tropical Pacific climate inferred from a Galápagos lake sediment record. *Quaternary Sci. Rev.* 27, 1166–1180.  
<https://doi.org/10.1016/j.quascirev.2008.02.015>.
- Dang, H., Jian, Z., Kissel, C., Bassinot, F., 2015. Precessional changes in the western

- equatorial Pacific hydroclimate: a 240 kyr marine record from the Halmahera Sea, East Indonesia. *Geochem. Geophys. Geosyst.* 16, 148–164. <https://doi.org/10.1002/2014GC005550>.
- de Garidel-Thoron, T., Beaufort, L., Linsley, B.K., Dannenmann, S., 2001. Millennial-scale dynamics of the East Asian winter monsoon during the last 200,000 years. *Paleoceanography* 16, 491–502. <https://doi.org/10.1029/2000PA000557>.
- Ding, Z., Liu, T., Rutter, N.W., Yu, Z., Guo, Z., Zhu, R., 1995. Ice-volume forcing of east asian winter monsoon variations in the past 800 000 years. *Quaternary Res.* 44, 149–159. <https://doi.org/10.1006/qres.1995.1059>.
- Groeneveld, J., Ho, S.L., Mackensen, A., Montagu, M., Laepple, T., 2019. Deciphering the Variability in Mg/Ca and Stable Oxygen Isotopes of Individual Foraminifera. *Paleoceanogr. Paleocl.* 34, 755–773. <https://doi.org/10.1029/2018PA003523>.
- Hao, Q., Wang, L., Oldfield, F., Guo, Z., 2015. Extra-long interglacial in Northern Hemisphere during MISs 15–13 arising from limited extent of Arctic ice sheets in glacial MIS 14. *Sci. Rep.* 5, 1–8. <https://doi.org/10.1038/srep12103>.
- Hao, Q., Wang, L., Oldfield, F., Peng, S., Qin, L., Song, Y., Xu, B., Qiao, Y., Bloemendal, J., Guo, Z., 2012. Delayed build-up of Arctic ice sheets during 400,000-year minima in insolation variability. *Nature* 490, 393–396. <https://doi.org/10.1038/nature11493>.
- Huang E., 2015. A comparison of the East Asian winter monsoon reconstructions from terrestrial and marine sedimentary records since the Mid-Pleistocene. *Quat. Sci.* 35, 1331–1341. <https://doi.org/10.11928/j.issn.1001-7410.2015.06.03>. (In Chinese with English Abstract)
- Huang, E., Tian, J., 2012. Sea-level rises at Heinrich stadials of early Marine Isotope Stage 3: Evidence of terrigenous n-alkane input in the southern South China Sea. *Glob. Planet. Change* 94–95, 1–12. <https://doi.org/10.1016/j.gloplacha.2012.06.003>.
- Huang, E., Tian, J., Steinke, S., 2011. Millennial-scale dynamics of the winter cold

- tongue in the southern South China Sea over the past 26ka and the East Asian winter monsoon. *Quaternary Res.* 75, 196–204. <https://doi.org/10.1016/j.yqres.2010.08.014>.
- Jackett, D.R., McDougall, T.J., Feistel, R., Wright, D.G., Griffies, S.M., 2006. Algorithms for density, potential temperature, conservative temperature, and the freezing temperature of seawater. *J. Atmos. Ocean. Tech.* 23, 1709–1728. <https://doi.org/10.1175/JTECH1946.1>.
- Jia, G., Bai, Y., Yang, X., Xie, L., Wei, G., Ouyang, T., Chu, G., Liu, Z., Peng, P., 2015. Biogeochemical evidence of Holocene East Asian summer and winter monsoon variability from a tropical maar lake in southern China. *Quaternary Sci. Rev.* 111, 51–61. <https://doi.org/10.1016/j.quascirev.2015.01.002>.
- Kalnay, E., Kanamitsu, M., Kistler, R., Collins, W., Deaven, D., Gandin, L., Iredell, M., Saha, S., White, G., Woollen, J., Zhu, Y., Chelliah, M., Ebisuzaki, E., Higgins, W., Janowiak, J., Mo, K.C., Kopelewski, C., Wang, J., Leetmaa, A., Reynolds, R., Jenne, R., Joseph, D., 1996. The NCEP/NCAR 40-year reanalysis project. *B. Am. Meteorol. Soc.* 77, 437–472. [https://doi.org/10.1175/1520-0477\(1996\)077%3C0437%3ATNYRP%3E2.0.CO%3B2](https://doi.org/10.1175/1520-0477(1996)077%3C0437%3ATNYRP%3E2.0.CO%3B2).
- Kang, S., Du, J., Wang, N., Dong, J., Wang, D., Wang, X., Qiang, X., Song, Y., 2020. Early Holocene weakening and mid- to late Holocene strengthening of the East Asian winter monsoon. *Geology* 48, 1043–1047. <https://doi.org/10.1130/G47621.1>.
- Koutavas, A., Joanides, S., 2012. El Niño-Southern Oscillation extrema in the Holocene and Last Glacial Maximum, *Paleoceanography* 27, PA4208, <https://doi:10.1029/2012PA002378>.
- Laj, C., Wang, P., Balut, Y., 2005. MD147-Marco Polo IMAGES XII Cruise Report. Institut Polaire Francais, pp. 36–38. <https://doi.org/10.17600/5200050>.
- Lambeck, K., Rouby, H., Purcell, A., Sun, Y., Sambridge, M., 2014. Sea level and global ice volumes from the Last Glacial Maximum to the Holocene. *Proc. Natl. Acad. Sci. U. S. A.* 111, 15296–15303. <https://doi.org/10.1073/pnas.1411762111>.

- Laskar, J., Fienga, A., Gastineau, M., Manche, H., 2011. La2010: a new orbital solution for the long-term motion of the Earth. *Astron. Astrophys.* 89, 1–15. <https://doi.org/10.1051/0004-6361/201116836>.
- Li, Q., Wu, H., Cheng, J., Zhu, S., Zhang, C., Wu, J., Lin, Y., Li, P., Ren, X., Zhao, D., Zhang, Y., 2021. Spatial variation of East Asian winter monsoon evolution between northern and southern China since the last glacial maximum. *Quaternary Res.* 103, 99–112. <https://doi.org/10.1017/qua.2020.101>.
- Lin, H.L., Sheu, D.D.D., Yang, Y., Chou, W.C., Hung, G.W., 2011. Stable isotopes in modern planktonic foraminifera: Sediment trap and plankton tow results from the South China Sea. *Mar. Micropaleontol.* 79, 15–23. <https://doi.org/10.1016/j.marmicro.2010.12.002>.
- Lisiecki, L.E., Raymo, M.E., 2005. A Pliocene-Pleistocene stack of 57 globally distributed benthic  $\delta^{18}\text{O}$  records. *Paleoceanography* 20, 1–17. <https://doi.org/10.1029/2004PA001071>.
- Liu, Q., Jiang, X., Xie, S.P., Liu, W.T., 2004. A gap in the Indo-Pacific warm pool over the South China Sea in boreal winter: Seasonal development and interannual variability. *J. Geophys. Res. Oceans* 109, 1–10. <https://doi.org/10.1029/2003JC002179>.
- Liu, T., Ding, Z., 1998. Chinese loess and the paleomonsoon. *Annu. Rev. Earth Pl. Sc.* 26, 111–145. <https://doi.org/10.1146/annurev.earth.26.1.111>.
- Liu, Z., Lu, Z., Wen, X., Otto-Bliesner, B.L., Timmermann, A., Cobb, K.M., 2014. Evolution and forcing mechanisms of El Niño over the past 21,000 years. *Nature* 515, 550–553. <https://doi.org/10.1038/nature13963>.
- Liu, Z., Otto-Bliesner, B.L., He, F., Brady, E.C., Tomas, R., Clark, P.U., Carlson, A.E., Lynch-Stieglitz, J., Curry, W., Brook, E., Erickson, D., Jacob, R., Kutzbach, J., Cheng, J., 2009. Transient simulation of last deglaciation with a new mechanism for bolling-allerod warming. *Science* 325, 310–314. <https://doi.org/10.1126/science.1171041>.
- Lu, H., Zhang, F., Liu, X., 2003. Patterns and frequencies of the East Asian winter monsoon variations during the past million years revealed by wavelet and

- spectral analyses. *Global Planet. Change* 35, 67–74. [https://doi.org/10.1016/S0921-8181\(02\)00136-4](https://doi.org/10.1016/S0921-8181(02)00136-4).
- Lu, Z., Liu, Z., Zhu, J., Cobb, K.M., 2018. A Review of Paleo El Niño-Southern Oscillation. *Atmosphere* 9, 130. <https://doi.org/10.3390/atmos9040130>.
- Luo, Q., Jin, H., Jian, Z., Wang, X., 2015. Vertical distribution of living planktonic foraminifera in the northern South China Sea and its paleoceanographic implications. *Quat. Sci.* 35, 1342–1353. <https://doi.org/10.11928/j.issn.1001-7410.2015.06.04>. (In Chinese with English Abstract).
- Moy, C.M., Seltzer, G.O., Rodbell, D.T., Anderson, D.M., 2002. Variability of El Niño/Southern Oscillation activity at millennial timescales during the Holocene epoch. *Nature* 420, 162–5. <https://doi.org/10.1038/nature01194>.
- Mulitza, S., Boltovskoy, D., Donner, B., Meggers, H., Paul, A., Wefer, G., 2003. Temperature:  $\delta^{18}\text{O}$  relationships of planktonic foraminifera collected from surface waters. *Palaeogeogr. Palaeoclimatol.* 202, 143–152. [https://doi.org/10.1016/S0031-0187\(03\)00633-3](https://doi.org/10.1016/S0031-0187(03)00633-3).
- Petit, J.R., Jouzel, J., Raynaud, D., Barkov, N.I., Barnola, J.-M., Basile, I., Bender, M., Chappellaz, J., Davisk, M., Delaygue, G., Delmotte, M., Kotlyakov, V.M., Legrand, M., Lipenkov, V.Y., Lorius, C., Pépin, L., Ritz, C., Saltzman, E., Stievenard, M., 1999. Climate and atmospheric history of the past 420,000 years from the Vostok ice core, Antarctica. *Nature* 399, 429–436. <https://doi.org/10.1038/20859>.
- Rayner, N.A., Parker, D.E., Horton, E.B., Folland, C.K., Alexander, L. V., Rowell, D.P., Kent, E.C., Kaplan, A., 2003. Global analyses of sea surface temperature, sea ice, and night marine air temperature since the late nineteenth century. *J. Geophys. Res. Atmos.* 108. <https://doi.org/10.1029/2002jd002670>.
- Sadekov, A.Y., Ganeshram, R., Pichevin, L., Berdin, R., McClymont, E., Elderfield, H., Tudhope, A.W., 2013. Palaeoclimate reconstructions reveal a strong link between El Niño-Southern Oscillation and Tropical Pacific mean state. *Nat. Commun.* 4. <https://doi.org/10.1038/ncomms3692>.
- Shaw, P.T., Chao, S.Y., 1994. Surface circulation in the South China Sea. *Deep-Sea*

- Res. PT. I 41, 1663–1683. [https://doi.org/10.1016/0967-0637\(94\)90067-1](https://doi.org/10.1016/0967-0637(94)90067-1).
- Shi, Z., Liu, X., Sun, Y., An, Z., Liu, Z., Kutzbach, J., 2011. Distinct responses of East Asian summer and winter monsoons to astronomical forcing. *Clim. Past* 7, 1363–1370. <https://doi.org/10.5194/cp-7-1363-2011>.
- Steinke, S., Glatz, C., Mohtadi, M., Groeneveld, J., Li, Q., Jian, Z., 2011. Past dynamics of the East Asian monsoon: No inverse behaviour between the summer and winter monsoon during the Holocene. *Global Planet. Change* 78, 170–177. <https://doi.org/10.1016/j.gloplacha.2011.06.006>.
- Stevens, T., Thomas, D.S.G., Armitage, S.J., Lunn, H.R., Jull, M., 2007. Reinterpreting climate proxy records from late Quaternary Chinese loess: A detailed OSL investigation. *Earth-Sci. Rev.* 80, 111–136. <https://doi.org/10.1016/j.earscirev.2006.09.001>.
- Sun, Y., An, Z., Clemens, S.C., 2010. Non-stationary response of Plio-Pleistocene East Asian winter monsoon variability to ice volume forcing. *Geol. Soc. Spec. Publ.* 342, 79–86. <https://doi.org/10.1144/SP342.7>.
- Sun, Y., Chen, J., Clemens, S.C., Liu, Q., Ji, J., Tada, R., 2006. East Asian monsoon variability over the last seven glacial cycles recorded by a loess sequence from the northwestern Chinese Loess Plateau. *Geochem. Geophys. Geosy.* 7, 1–16. <https://doi.org/10.1029/2006GC001287>.
- Tian, J., Huang, E., Pak, D.K., 2010. East Asian winter monsoon variability over the last glacial cycle: Insights from a latitudinal sea-surface temperature gradient across the South China Sea. *Palaeogeogr. Palaeoclimatol.* 292, 319–324. <https://doi.org/10.1016/j.palaeo.2010.04.005>.
- Tian, Z., Jiang, D., 2018. Strengthening of the East Asian winter monsoon during the mid-Holocene. *Holocene* 28, 1443–1451. <https://doi.org/10.1177/0959683618777076>.
- Waelbroeck, C., Labeyrie, L., Michel, E., Duplessy, J.C., McManus, J.F., Lambeck, K., Balbon, E., Labracherie, M., 2002. Sea-level and deep water temperature changes derived from benthic foraminifera isotopic records. *Quaternary Sci. Rev.* 21, 295–305. [https://doi.org/10.1016/S0277-3791\(01\)00101-9](https://doi.org/10.1016/S0277-3791(01)00101-9).

- Wan, S., Jian, Z., 2014. Deep water exchanges between the South China Sea and the Pacific since the last glacial period. *Paleoceanography* 29, 1162–1178. <https://doi.org/10.1002/2013PA002578>.
- Wan, S., Jian, Z., Cheng, X., Qiao, P., Wang, R., 2010. Seasonal variations in planktonic foraminiferal flux and the chemical properties of their shells in the southern South China Sea. *Sci. China Earth Sci.* 53, 1176–1187. <https://doi.org/10.1007/s11430-010-4039-3>.
- Wang, L., Li, J., Lu, H., Gu, Z., Rioual, P., Hao, Q., Mackay, A.W., Jiang, W., Cai, B., Xu, B., Han, J., Chu, G., 2012. The East Asian winter monsoon over the last 15,000 years: Its links to high-latitudes and tropical climate systems and complex correlation to the summer monsoon. *Quaternary Sci. Rev.* 32, 131–142. <https://doi.org/10.1016/j.quascirev.2011.11.003>.
- Wen, X., Liu, Z., Wang, S., Cheng, J., Zhu, J., 2016. Correlation and anti-correlation of the East Asian summer and winter monsoons during the last 21,000 years. *Nat. Commun.* 7, 11999. <https://doi.org/10.1038/ncomms11999>.
- Xie, X., Liu, X., Chen, G., Kory, R.L., 2019. A transient modeling study of the latitude dependence of East Asian winter monsoon variations on orbital timescales. *Geophys. Res. Lett.* 46, 7565–7573. <https://doi.org/10.1029/2019GL083060>.
- Yamamoto, M., Sai, H., Chen, M., Zhao, M., 2013. The East Asian winter monsoon variability in response to precession during the past 150 000 yr. *Clim. Past* 9, 2777–2788. <https://doi.org/10.5194/cp-9-2777-2013>.
- Yang, S., Ding, Z., 2014. A 249 kyr stack of eight loess grain size records from northern China documenting millennial-scale climate variability. *Geochem. Geophys. Geosy.* 15, 798–814. <https://doi.org/10.1002/2013GC005113>.
- Zhang, Y., Zhu, K., Huang, C., Kong, D., He, Y., Wang, H., Liu, W., Xie, Z., Wei, G., Liu, Z., 2019. Asian winter monsoon imprint on Holocene SST changes at the northern coast of the South China Sea. *Geophys. Res. Lett.* 46, 13363–13370. <https://doi.org/10.1029/2019GL085617>.
- Zhang, Z., Leduc, G., Sachs, J.P., 2014. El Niño evolution during the Holocene



revealed by a biomarker rain gauge in the Galápagos Islands. *Earth Planet. Sci. Lett.* 404, 420–434. <https://doi.org/10.1016/j.epsl.2014.07.013>.

Zhao, D., Wan, S., Song, Z., Gong, X., Zhai, L., Shi, X., Li, A., 2019. Asynchronous variation in the Quaternary East Asian winter monsoon associated with the tropical Pacific ENSO-like system. *Geophys. Res. Lett.* 46, 6955–6963. <https://doi.org/10.1029/2019GL083033>.

### Figure caption

Fig.1 Modern East Asian climatology. (a) December-January-February (DJF) 1000 mPa winds. (b) June-July-August (JJA) and (c) DJF ocean surface currents and SST distribution over the SCS. Wind and SST data are mean values for the period 1949-2021, derived from the NCEP/NCAR Reanalysis Project (Kalnay et al., 1996). Surface currents are mean values for the period 1980-2010, based on the SODA3.32 database (Jackett et al., 2006). Locations of cores MD05-2896/97 and a sediment trap are indicated.

Fig.2 Comparison of the SCS DJF wind speed with the southern SCS seasonal SST contrast (a) and the monthly Niño 3.4 SST anomaly (b) for the period 1949-2022. The DJF meridional wind speeds at 1000 mPa are weighted averages for the region 10°-20°N, 110°-120°E (indicated by a rectangle in Fig.1a). The winter monsoon wind speeds in this region largely determine the winter SST distribution of the SCS, which thus show a significant correlation with the seasonal SST contrast at the core locations of MD05-2896/97. The JJA-DJF SST differences are weighted averages for the region 8.5°-10°N, 110.5°-112.5°E (indicated by a rectangle in Fig.1b). The latter region includes the core location of MD05-2896/97. Both wind and SST data are derived from the NCEP/NCAR Reanalysis Project (Kalnay et al., 1996). The Niño 3.4 SST results are from Rayner et al. (2003). Note that the DJF meridional wind speeds are

negative values.

Fig.3 Monthly flux and  $\delta^{18}\text{O}$  changes of *G. ruber* in the southern SCS based on a sediment-trap record. The grey rectangles in (a) indicate relatively high fluxes of *G. ruber* during both the summer and winter monsoon seasons. (b) *G. ruber*  $\delta^{18}\text{O}$  from shallow and deep traps show consistent changes, indicating that the lateral transport in the SCS has no evident impact on sedimentary *G. ruber*  $\delta^{18}\text{O}$  signals. Sediment-trap data are from Wan et al. (2010). (c) Monthly-mean SST data at the sediment-trap location are derived from the NCEP/NCAR Reanalysis Project (Kalnay et al., 1996).

Fig.4 Pooled- and individual-specimen  $\delta^{18}\text{O}$  of *G. ruber* for MISs 1 and 5e at site MD05-2896/97. (a) *C. wuellerstorfi*  $\delta^{18}\text{O}$  for the past 140 thousand years with AMS  $^{14}\text{C}$  dating position indicated by triangles. (b and d) Comparison of pooled- (orange) and individual-specimen (dark blue)  $\delta^{18}\text{O}$  of *G. ruber*. Mean values of individual-specimen  $\delta^{18}\text{O}$  are indicated by large blue dots. (c and e) Comparison of the standard deviation of individual-specimen  $\delta^{18}\text{O}$  (blue dots) with precession (dark red, Laskar et al., 2011). The thick blue curves are third-degree polynomial fits to the individual-specimen  $\delta^{18}\text{O}$  results, while the thin blue curves indicate 95% confidence levels for the polynomial fits.

Fig.5 Comparison of the Holocene EAWM records with the ENSO evolution. (a) The southern EAWM reconstruction based on individual-specimen  $\delta^{18}\text{O}$  (blue dots, this study). The thick blue curve is a third-degree polynomial fit to the individual-specimen  $\delta^{18}\text{O}$  results, while the thin blue curves indicate 95% confidence levels for the polynomial fit. (b) The southern EAWM reconstruction according to the annual SST gradient between the southwestern and southeastern SCS (Huang et al., 2011). (c-d) The northern EAWM reconstructions based on loess grain-size variations. The two stacks are adopted from Yang and Ding (2014, CHILOMOS) and Kang et al. (2020), respectively. (e) December 21 insolation at 50°N (Laskar et al., 2011). (f) Reconstructed changes in the ENSO dynamics. Number of El Niño events per 100

years recorded at Laguna Pallcacocha, Ecuador (light blue, Moy et al., 2002). Percentage of sand fraction in lacustrine sediments from the Galápagos Islands, eastern Pacific (red, Conroy et al., 2008). (g) Simulated changes in annual-mean SST over the Niño 3.4 region, derived from the integrated TRACE-21 experiment (Liu et al., 2014).

Fig.6 Forcing mechanisms for the tropical EAWM changes over the Holocene according to the TRACE-21 experiments. (a) Comparison of the southern EAWM reconstructions (blue dots) with the simulated DJF wind speeds at 1000 mPa over the SCS (dark red). The thick blue curve is a third-degree polynomial fit to the individual-specimen  $\delta^{18}\text{O}$  results, while the thin blue curves indicate 95% confidence levels for the polynomial fit. The model outputs are from the integrated experiment. (b) Comparison of the simulated DJF wind speeds at 1000 mPa from different experiments. These experiments are solely forced by orbital parameters (light blue), greenhouse-gas concentrations (red), continental ice sheets (orange) and meltwater fluxes (black). All simulated DJF wind speeds are weighted averages for the  $10^{\circ}$ - $20^{\circ}\text{N}$ ,  $110^{\circ}$ - $120^{\circ}\text{E}$  region indicated by a rectangle in Fig.1a. Note that the simulated DJF meridional wind speeds are negative values.

Fig.7 The simulated winter wind field (DJF) at 1000 mPa over East Asia and the North Pacific, derived from the integrated TRACE-21 experiment. (a) Mean wind field during the late Holocene (1-0 ka BP). (b) The mean wind field difference between the early (11-10 ka BP) and late Holocene (1-0 ka BP). Both the northern and southern modes of the EAWM show a stronger intensity during the early Holocene compared to the late Holocene. The northern EAWM was strengthened due to a combined influence of precession, residual ice sheets and greenhouse-gas concentrations (Li et al., 2021), while the southern EAWM was enhanced driven by precessional forcing alone. Red arrows indicate the anomalous cyclonic circulation induced by the suppressed El Niño activity during the early Holocene.

## Tables

**Table 1** Summary of individual-specimen  $\delta^{18}\text{O}$  measurements from cores MD05-2896 and 2897 after removal of outliers

Core	Core Depth (cm)	Age (ka)	NO. of analyses	mean $\delta^{18}\text{O}$ (PDB, ‰)	standard deviation of $\delta^{18}\text{O}$	<i>p</i> value of Lilliefors test *
MD05-2896	1.5	0.73	37	-3.293	0.221	0.471
MD05-2896	5.5	1.23	36	-3.201	0.259	0.101
MD05-2896	9.5	1.72	41	-3.096	0.377	0.141
MD05-2896	27.5	3.98	36	-3.260	0.191	0.113
MD05-2896	31.5	4.49	34	-3.316	0.222	0.460
MD05-2896	33.5	4.74	38	-3.181	0.376	0.500
MD05-2896	47.5	6.52	39	-3.220	0.413	0.278
MD05-2896	57.5	7.67	45	-2.872	0.506	0.500
MD05-2896	61.5	8.11	36	-3.050	0.357	0.006
MD05-2896	65.5	8.56	50	-3.002	0.447	0.055
MD05-2896	75.5	9.68	37	-3.270	0.461	0.500
MD05-2896	85.5	11.47	36	-2.659	0.523	0.500
MD05-2896	87.5	12.02	37	-2.568	0.439	0.169
MD05-2897	919.5	117.15	34	-2.763	0.225	0.500
MD05-2897	931.5	118.87	38	-3.127	0.246	0.494
MD05-2897	937.5	119.74	39	-3.313	0.306	0.371
MD05-2897	943.5	120.6	37	-3.381	0.321	0.500
MD05-2897	951.5	121.77	35	-3.286	0.435	0.500
MD05-2897	957.5	122.54	42	-3.206	0.610	0.017
MD05-2897	963.5	123.51	33	-3.350	0.479	0.045
MD05-2897	969.5	124.38	37	-3.319	0.356	0.153
MD05-2897	977.5	125.54	36	-3.166	0.599	0.306
MD05-2897	983.5	126.41	36	-3.043	0.636	0.158

\**p* value of the Lilliefors test for normality, with  $P > 0.05$  indicating a normal distribution of the individual-specimen  $\delta^{18}\text{O}$  measurements in a given sample.

### **Declaration of interests**

The authors declare that they have no known competing financial interests or personal relationships that could have appeared to influence the work reported in this paper.

### **Highlights**

Reliable monsoon reconstruction based on spreading of single specimen oxygen isotopes

Transient simulations give clear mechanisms for winter monsoon evolution

Boreal winter insolation determines wind intensity via altering temperature gradient

A tight correlation between tropical winter monsoon and ENSO dynamics

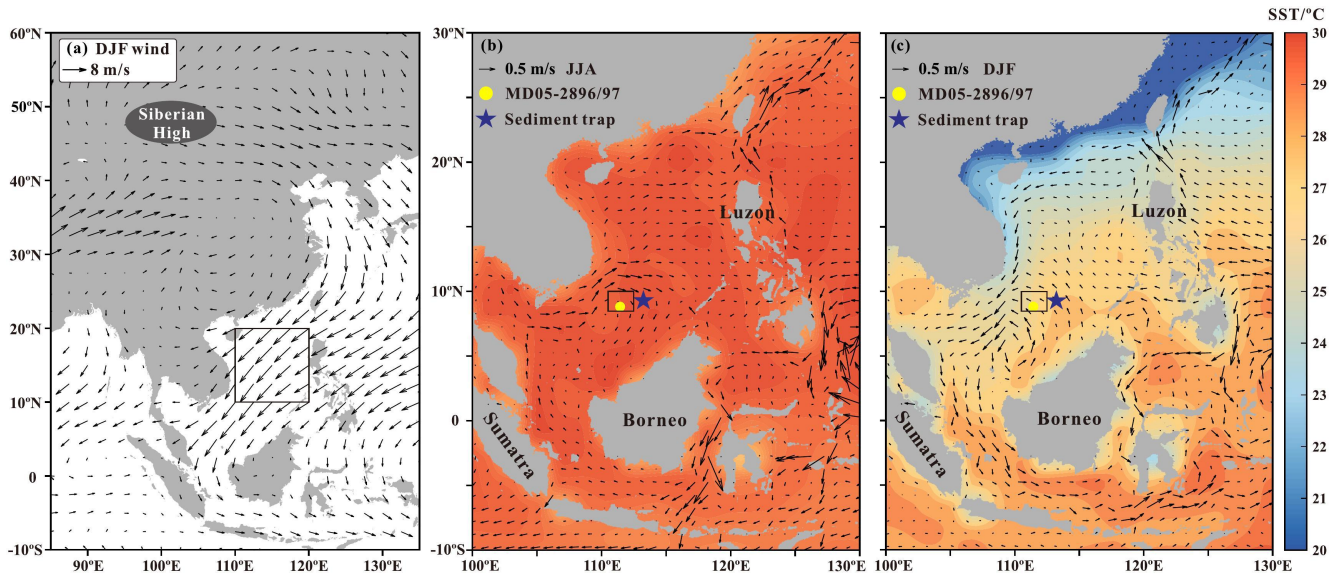


Figure 1

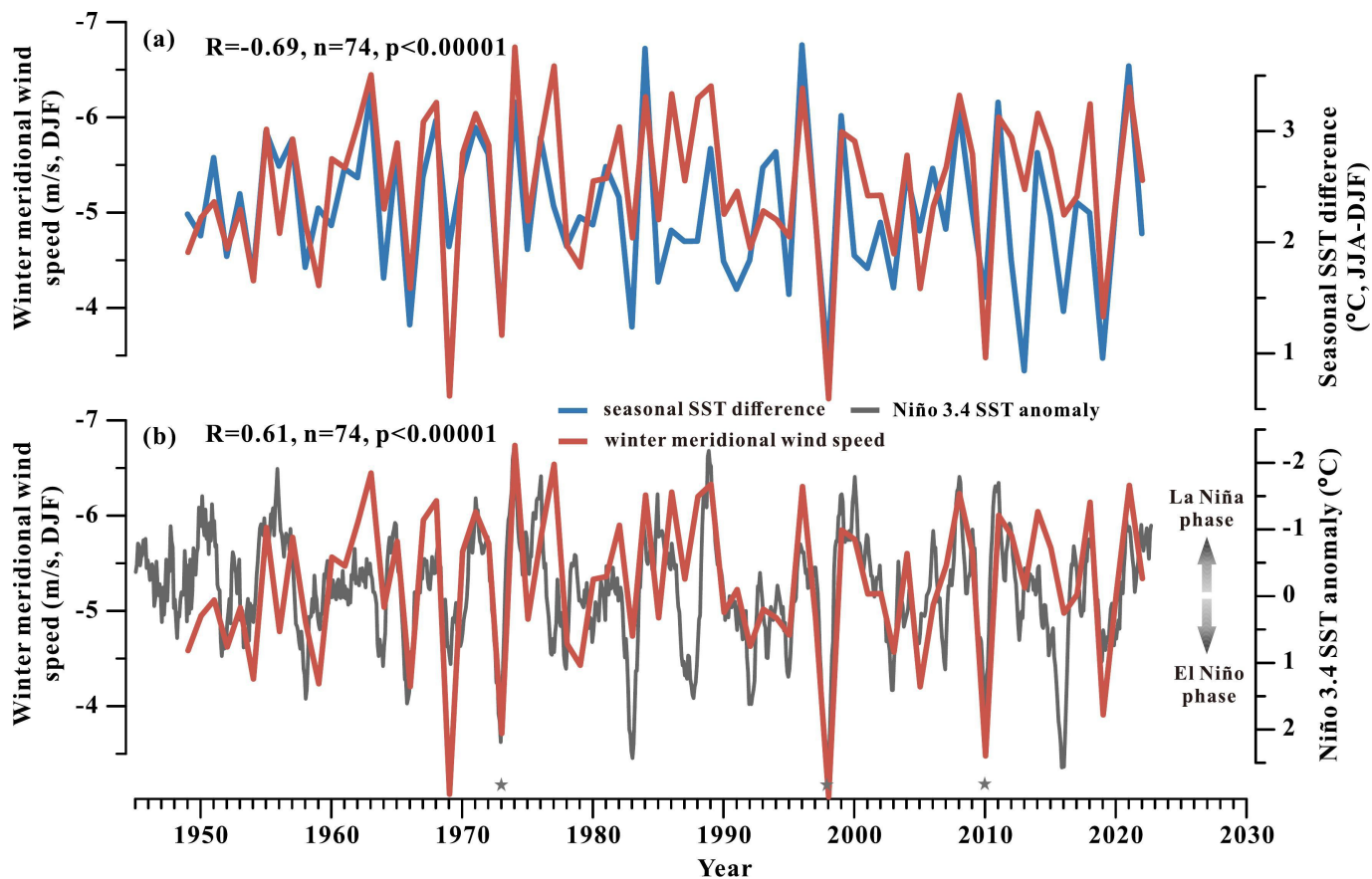


Figure 2

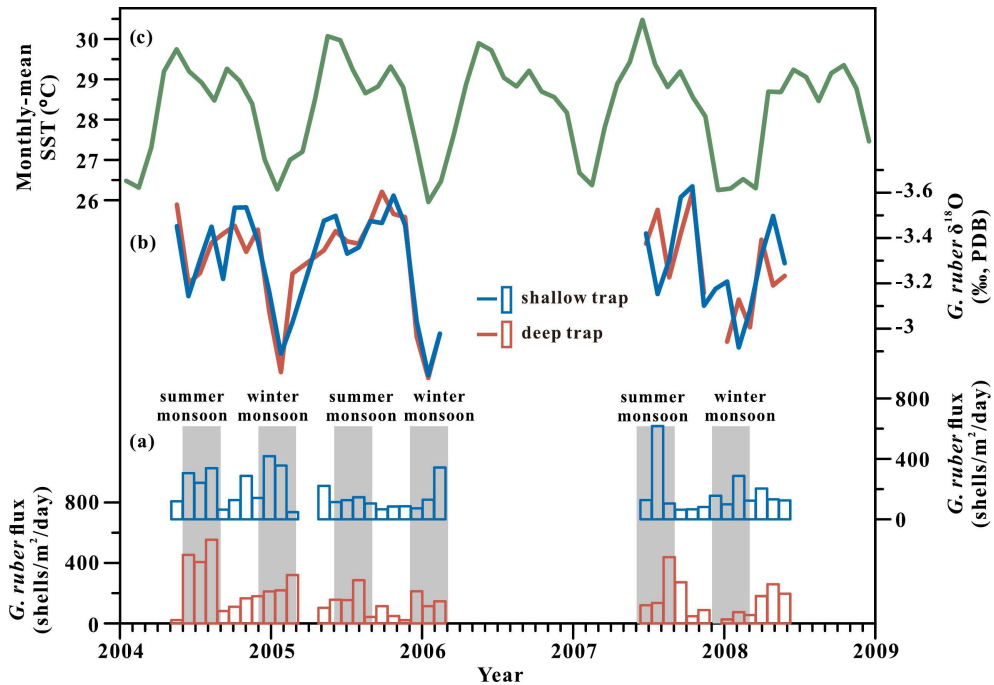


Figure 3



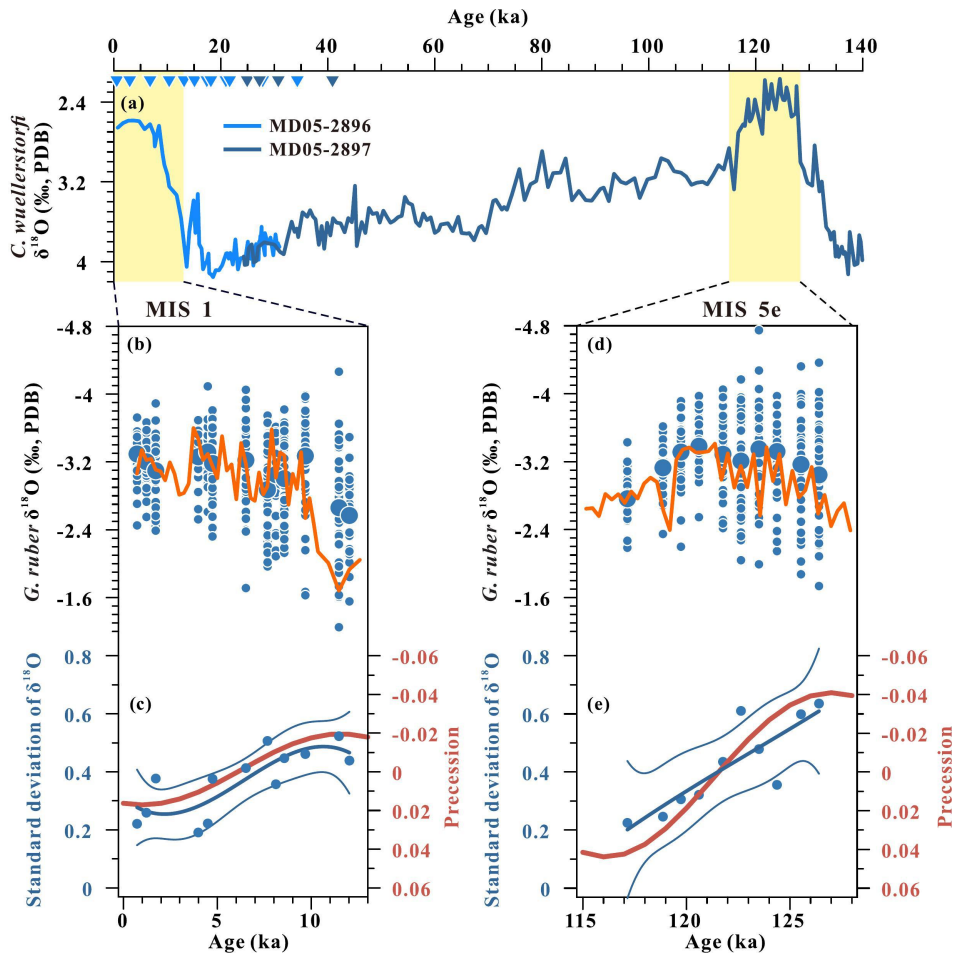


Figure 4

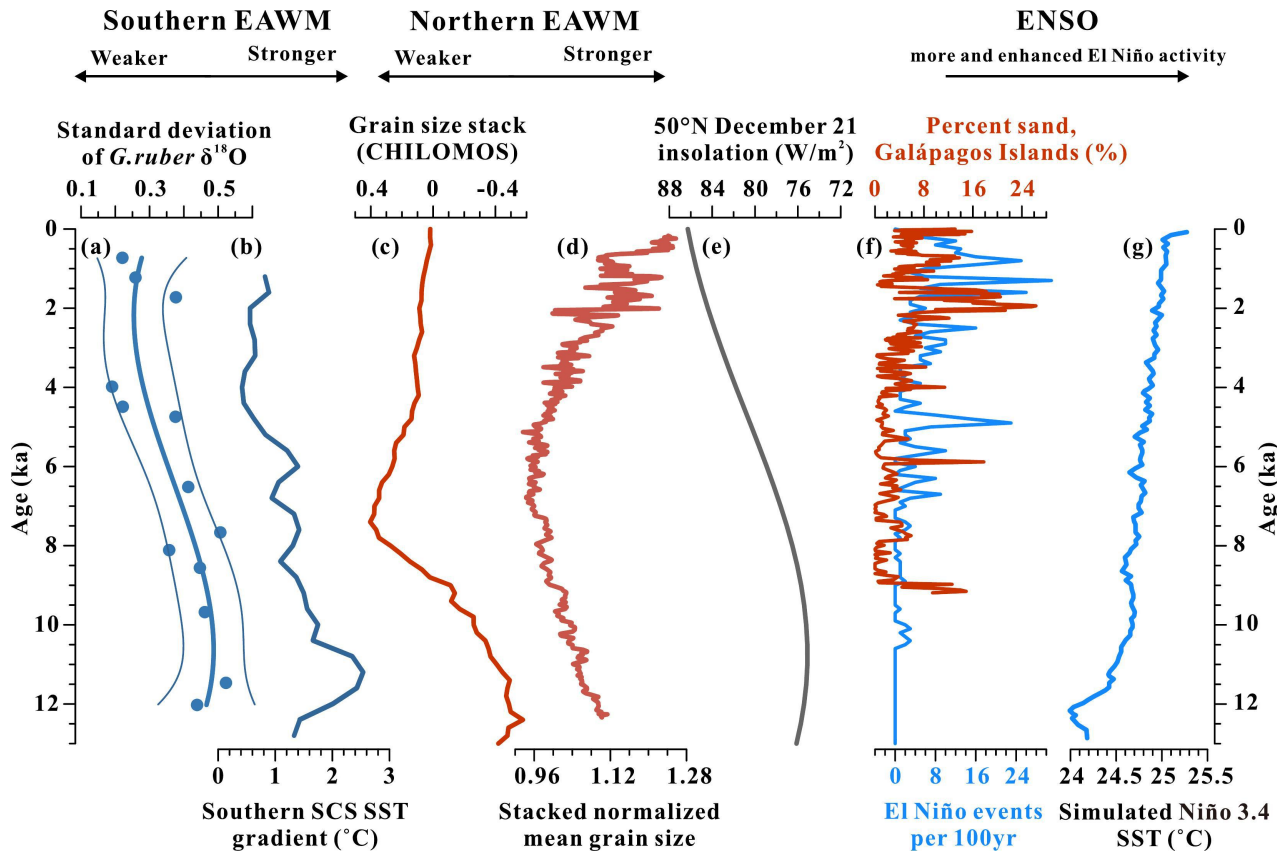


Figure 5

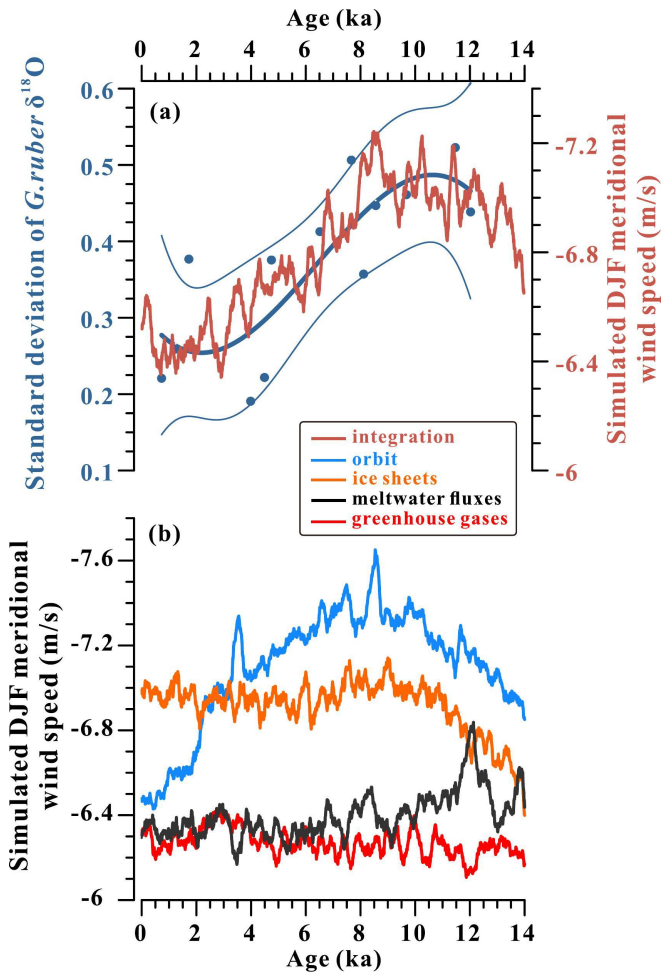
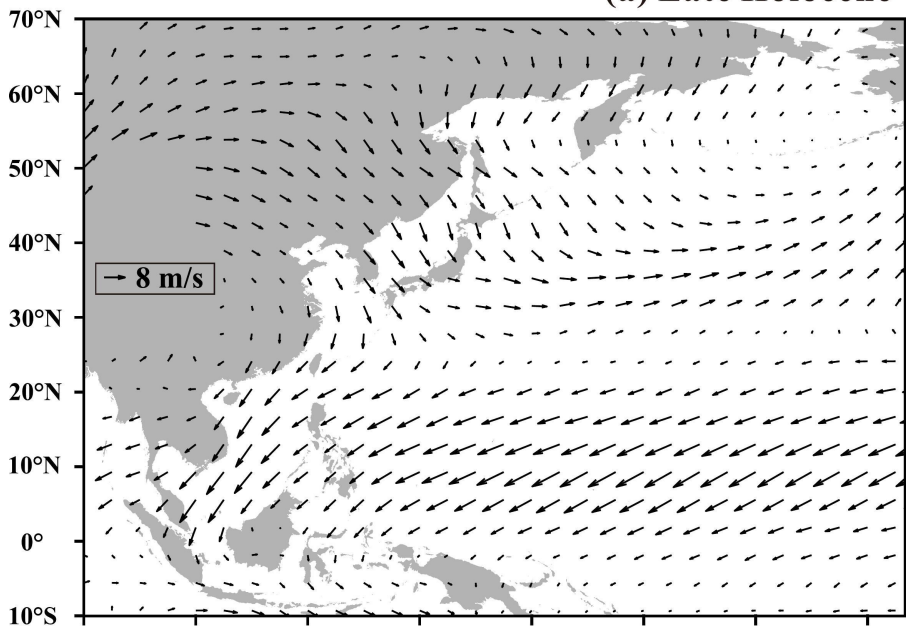


Figure 6

**(a) Late Holocene**



**(b) Early-Late Holocene**

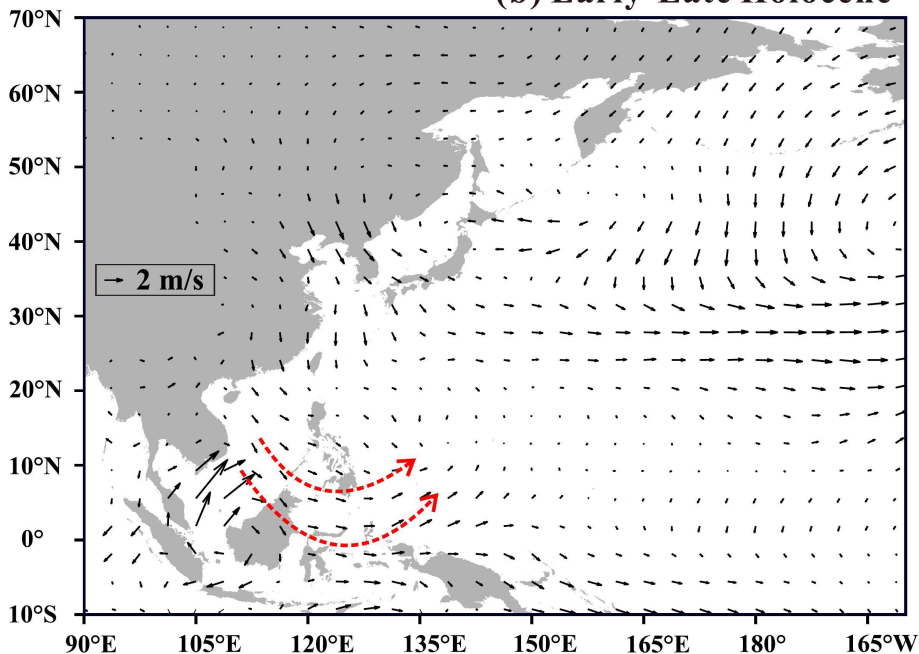


Figure 7